Journal of
Materials Chemistry A

Materials for energy and sustainability

Accepted Manuscript

This article can be cited before page numbers have been issued, to do this please use: R. Keshavarzi, F. Hajisharifi, P. Golabi, R. Sheibani and A. Dabirian, *J. Mater. Chem. A*, 2025, DOI: 10.1039/D5TA01376C.

ROYAL SOCIETY OF CHEMISTRY

rsc.li/materials-a

View Article Online
DOI: 10.1039/D5TA01376C

ARTICLE

Highly Efficient and Stable $CsPbBr_3$ Perovskite Photoanodes Based on Inverse Opal TiO_2 Layers in Photoelectrochemical Water Splitting

Reza Keshavarzi,*[a] Farzaneh Hajisharifi,[a] Parisa Golabi,[a] Reza Sheibani,[b] and Ali Dabirian[c]

[a] *Department of Chemistry, University of Isfahan, Isfahan 81746-73441, Iran*

[b] *Amirkabir University of Technology-Mahshahr Campus, Nahiyeh san'ati, Mahshahr, Khouzastan, Iran*

[c] *Optic Niroo Ltd., Shamsipour Technical and Vocational College Incubator, Tehran, Iran*

Received 00th January 20xx,
Accepted 00th January 20xx

DOI: 10.1039/x0xx00000x

$CsPbBr_3$, an inorganic halide perovskite compound, has attracted significant attention in the photoelectrochemical water splitting (PEC-WS) process due to its excellent properties; i.e. low cost, processing at ambient temperature and humidity, tunable bandgap, and long carrier transport length. Despite its intrinsically good optoelectronic properties, the practical optical absorption of thin $CsPbBr_3$ films could be improved, particularly near the optical absorption edge, to obtain high photocurrent densities in PEC-WS applications. In this regard, we propose and validate the use of inverse-opal nanostructure of TiO_2 (IOT) electron transport layer as a scaffold for $CsPbBr_3$ in water splitting devices. We observed that using IOT improves PEC-WS performance mainly due to two effects: i) improved light absorption near the optical absorption edge and ii) enhanced charge transfer within the electrode associated mainly to the shortened path of electron transport within the perovskite layer. Moreover, the $CsPbBr_3$ widespread application is hindered by limited durability in aqueous environments. A carbon ink composed of conductive carbon black, graphite, and a waste carbon toner is applied onto the perovskite layer to improve its stability in the electrolyte and to enhance charge injection from the electrode into the electrolyte. A high photocurrent density of 7.28 $mA.cm^{-2}$ at 1.23 V vs reversible hydrogen electrode (RHE) was obtained and maintained for 10000 s at pH=7 for the photoanode with the configuration of Glass/FTO/Compact-TiO_2/Mesoporous-TiO_2/Inverse Opal TiO_2/$CsPbBr_3$/C without using any co-catalyst.

Introduction

Excessive exploitation of non-renewable fossil fuels has increased atmospheric CO_2 levels to a high record (420 ppm in 2023), which requires urgent action to reduce severe environmental and climate impacts [1-3]. The increasing pollution of the environment and on the other hand the deficiency of energy have multiplied the need for clean and renewable energy [4-6]. Hydrogen gas (H_2) has become a green energy source due to its high gravimetric energy density (141.9 MJ kg^{-1}) and the absence of CO_2 gas production during combustion, which can solve the challenges related to the energy crisis [7-9]. The methods currently used to produce hydrogen, such as water electrolysis [10-12] and methane reforming [13-15], consume large amounts of fossil fuels and electricity [16, 17]. Solar energy is an abundant and inexhaustible source of energy that can be used for hydrogen generation. In this regard, using sunlight and water through a process called photoelectrochemical water splitting (PEC-WS) to produce hydrogen and oxygen has attracted widespread attention [18-23]. Among the advantages of the PEC-WS method, easy separation of products, simple manufacturing process, high theoretical yield, and low cost can be mentioned.

Among semiconductors for PEC-WS, inorganic halide perovskites like $CsPbBr_3$ are highly attractive due to their tunable bandgap (2.3 eV), long carrier diffusion lengths, and low-cost ambient processing [24-27]. However, the present performance of $CsPbBr_3$ photoanodes has the potential for improvement by i) enhancing optical absorption in $CsPbBr_3$ thin films, ii) increasing the material durability in aqueous electrolytes, and iii) optimizing charge transport dynamics.

To address these challenges, we use an inverse opal TiO_2 (IOT) scaffold integrated with $CsPbBr_3$ photoanodes. The IOT structure, a three-dimensional photonic crystal, enhances

† Footnotes relating to the title and/or authors should appear here.
Electronic Supplementary Information (ESI) available: [details of any supplementary information available should be included here]. See DOI: 10.1039/x0xx00000x

visible-light absorption through precise control of light propagation [28]. The periodic arrangement of interconnected pores in the IOT creates photonic bandgaps, regions in the electromagnetic spectrum where light propagation is inhibited, leading to enhanced light confinement within the structure [29]. This confinement increases the effective optical path length, amplifying photon-semiconductor interactions and boosting electron-hole pair generation. The high surface area of the IOT's porous framework further facilitates efficient charge extraction by providing a large interfacial area for carrier collection. Additionally, a conductive carbon-based protective layer, composed of conductive carbon black, graphite, and a carbon waste toner, stabilizes the perovskite-electrolyte interface and hence improves hole injection into the electrolyte. This synergistic design improves optical absorption, stability, and charge transport, enabling high-performance $CsPbBr_3$-based photoanodes for PEC-WS.

In this regard, we processed IOT layers on top of a mesoporous TiO_2 (m-TiO_2) and a compact TiO_2 (c-TiO_2) film followed by deposition of $CsPbBr_3$ in two different configurations: i) FTO/c-TiO_2/m-TiO_2/IOT/$CsPbBr_3$/C and, ii) FTO/c-TiO_2/IOT/$CsPbBr_3$/C to use in PEC water oxidation. The structural properties of the samples were characterised by XRD, SEM, and EDS. The functional properties were measured using UV-vis optical absorption, linear sweep voltammetry, chronoampermetry, incident photon conversion efficiency (IPCE) measurement, photo-luminescence spectroscopy and electrochemical impedance spectroscopy (EIS).

Experimental Section

Preparation of c-TiO_2 and m-TiO_2 layers

Fluorine-doped tin oxide (FTO) conductive glass substrates (15Ω/sq, Solaronix) were sonicated sequentially in soap/deionized (DI) water, DI water, 0.1 M HCl, acetone, ethanol, and 2-propanol solutions for 10 min and then dried in air. Next, the substrates were immersed in a Piranha solution (33.3% (v/v) of H_2SO_4 and H_2O_2) for 30 min and dried again. After that, they were treated with UV-ozone for 15 min. A compact TiO_2 (c-TiO_2) layer was deposited by spin-coating a solution of 1.4% (v/v) titanium isopropoxide (97 wt%, Merck) in ethanol (96 wt%, Merck), and 1.3% (v/v) HCl (37 wt%, Merck) in ethanol at 2000 rpm and then annealing the samples at 500°C for 1 h in a furnace. A mesoporous TiO_2 (m-TiO_2) layer was deposited by spin-coating a mixture of 0.015% (w/v) TiO_2 paste (20 nm, Sharif Solar) in ethanol at 4000 rpm and then drying the samples at 100 ºC for 10 min followed by annealing at 500 °C for 30 min with a ramp rate of 5 °C/min.

Self-assembly of opals

The self-assembly of opals were carried out according to our previous work [28]. In this regard, Polystyrene (PS) monodisperse spheres (400 nm diameter; 10 wt% in water, Merck) were selected as precursor. The PS spheres were diluted to 0.82 % (v/v) in ultrapure water and then, Triton X-100 (15 µL for 2.5 mL of PS solution, Merck) was added dropwise to the PS solution. After placing substrates at a 60° angle into vials on a hotplate at a temperature of 55°C, the PS colloidal suspension was added until the evaporation of the solution and self-assembly were completed.

Processing of IOT layer

Liquid-phase deposition method (LPD) was used to prepare the IOT films. In the LPD method, the seeding step is carried out as follows:

$$Ti(OCH(CH_3)_2)_4 + 4H_2O/H^+ \rightarrow Ti(OH)_4 + TiO_2 + 2H_2O \quad (1)$$

$$2TiF_6^{2-} + 3BO_3^{3-} + 10H^+ \rightarrow 3BF_4^- + 2TiO_2 + 5H_2O \quad (2)$$

In the seeding stage, 0.15% (w/v) titanium (IV) isopropoxide in ethanol was added to a solution of 0.015% (w/v) HNO_3 (Merck, 65%) in water and was stirred for 15 min. The obtained solution was poured into the vials containing vertically placed opal samples. In the LPD step, a solution of 0.1 M $(NH_4)_2TiF_6$ (Sigma-Aldrich) and 0.2 M H_3BO_3 (Merck) was made at 50 ºC and at pH=2.9 by the addition of 1 M HCl (37 wt%, Merck). The samples were immersed in the obtained solution. Then, the layered materials were carefully washed with ultrapure water and dried in ambient air for 1 h. A programmable furnace at 450 °C for 9 h was used to remove the PS template.

Perovskite and carbon layer deposition

A two-step method was used for the perovskite layer deposition. First, 0.39% (w/v) $PbBr_2$ in Dimethylformamide (DMF) was prepared at 70 °C and separately 1.7% (w/v) CsBr in methanol (99.6 wt%, Merck) was prepared at 50 °C inside a glovebox. The $PbBr_2$ solution was deposited on substrates preheated at 70 ºC by spin-coating at 2500 rpm. Then, deposited layer immersed in CsBr solution for 30 min and then annealed at 450 °C for 1 h. For the carbon film, a mixture of conductive carbon black, graphite, carbon waste toner (canon) in a weight ratio of 0.25:1:2 was dissolved in ethyl methyl ketone solvent. Next, the prepared ink was coated by Dr. Blade method and allowed to dry at ambient temperature. To prevent the direct contact of the electrolyte with the perovskite, the edges of the photoanode were sealed, as seen in the Fig. S1.

Characterization

A field emission scanning electron microscope (FE-SEM, S4160 Hitachi Japan) was used to examine the surface morphology and thickness of layers. The optical properties of the deposited layers were studied using a UV/Vis/NIR Spectrometer (Shimadzu, M160). Incident Photon-to-current conversion efficiency (IPCE) measurements were performed with the ON-

View Article Online
TA01376C

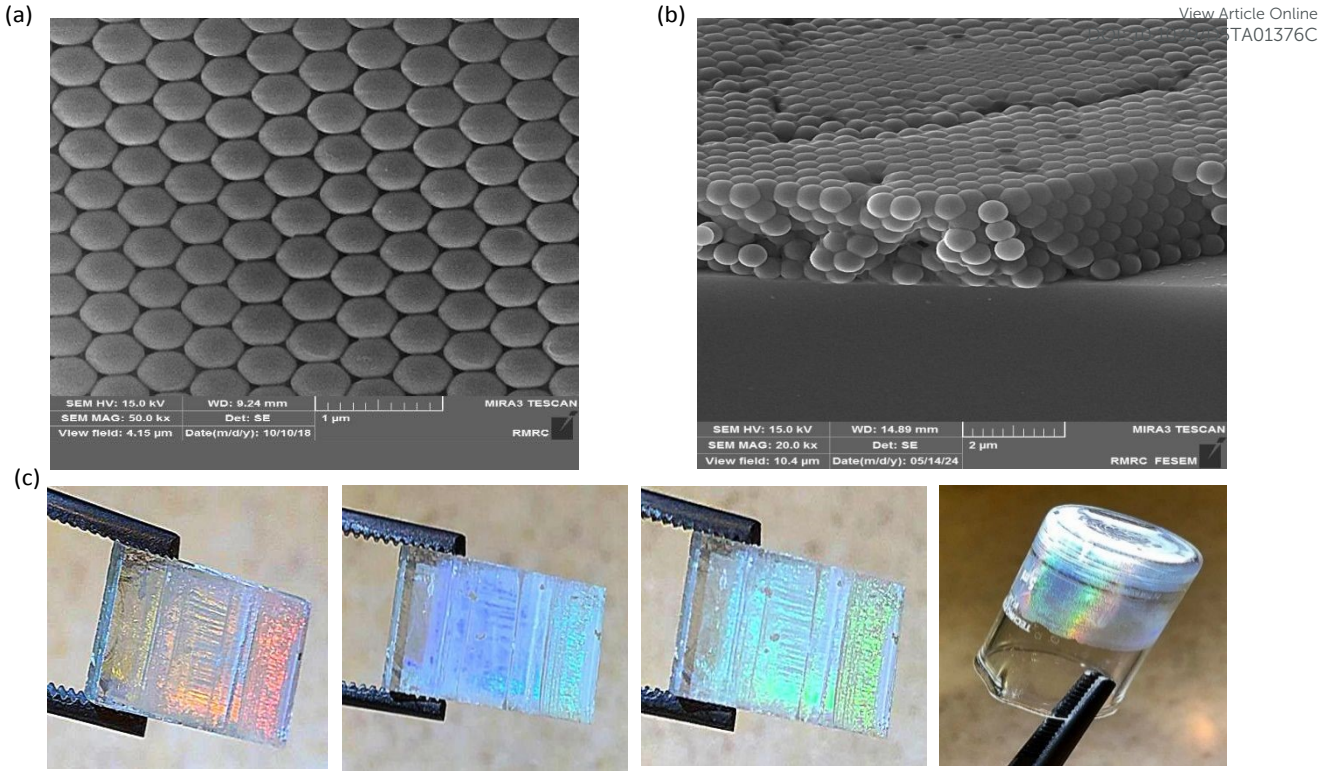

Fig. 1 (a) FE-SEM top-view and (b) cross-sectional view images of initial opals formed from 400 nm PS spheres. (c) The reflection camera images of the PS opals on the FTO substrates, and bottom of the vial used for deposition.

EQE-20 equipment (Optic Niroo Ltd. Iran). A spectrophotometer (Shimadzu, RF-5000) was used to measure the amount of light absorption by measuring the light intensity when the light beam passes through. The crystalline phase of the TiO_2 inverse opal films was characterized using XRD technique with a Bruker D8 Advance X-ray diffractometer, Cu Kα source, λ= 1.540598 ºA. An electrochemical workstation (OCTOSTAT5000) under simulated solar light irradiation (Optic Niroo, AM1.5G, 100 $mWcm^{-2}$) was used for PEC measurements. Using Electrochemical Impedance Spectroscopy (EIS), the charge transfers characteristics at 1.23 V_{RHE} were investigated with a frequency range from 10^{-2} Hz to 10^5 Hz and an AC amplitude of 10 mV in the dark by an AUTOLAB PGSTAT302N Metrohm Potentiostat.

Photoelectrochemical performance measurements

Photoelectrochemical measurements were carried out for C-PSC based photoanodes with an active surface of 0.09 cm^2 as the working electrode (WE), Pt wire as counter electrode (CE) and Ag/AgCl electrode as reference electrode (RE) in a 0.1 M Na_2SO_4 electrolyte solution with pH=7.

Results and discussion:

Photoanodes involved in this work include four structures Glass/FTO/c-TiO_2/m-TiO_2/IOT/$CsPbBr_3$/C, Glass/FTO/c-TiO_2/IOT/$CsPbBr_3$/C, Glass/FTO/c-TiO_2/m-TiO_2/$CsPbBr_3$/C, Glass/FTO/c-TiO_2/$CsPbBr_3$/C. These configurations are denoted as m-TiO_2/IOT/PVSK, c-TiO_2/IOT/PVSK, m-TiO_2/PVSK, and c-TiO_2/PVSK, respectively.

Characterization of Opals

The great degree of order in the self-assembly of 3D PC templates was revealed by cross sectional and top view FE-SEM images of PS spheres on the substrate (Fig. 1a and 2b). The top view images reveal the PS spheres to be perfectly regular with a face-centered cubic (f.c.c.) alignment along the close-packed (111) lattice planes oriented parallel to the substrate [30]. However, scanning electron micrographs confirm the successful synthesis of 3D polystyrene PC template. The primary opal structure, composed of 400 nm polystyrene (PS) spheres in a periodic arrangement, serves as a template for the inverse opal TiO_2 (IOT) scaffold. After TiO_2 infiltration and PS spheres removal, the resulting IOT structure forms a photonic bandgap that enhances light confinement, increasing the optical path length and amplifying photon absorption by the $CsPbBr_3$ layer integrated within it. The slow-photon effect at bandgap edges further boosts electron-hole pair generation for photoelectrochemical water splitting. Photographs of the opal films (Fig. 1c) show color changes due to photonic bandgap, indicating high structural quality of the opal PS template [28, 31-37].

View Article Online
DOI: 10.1039/D5TA01376C

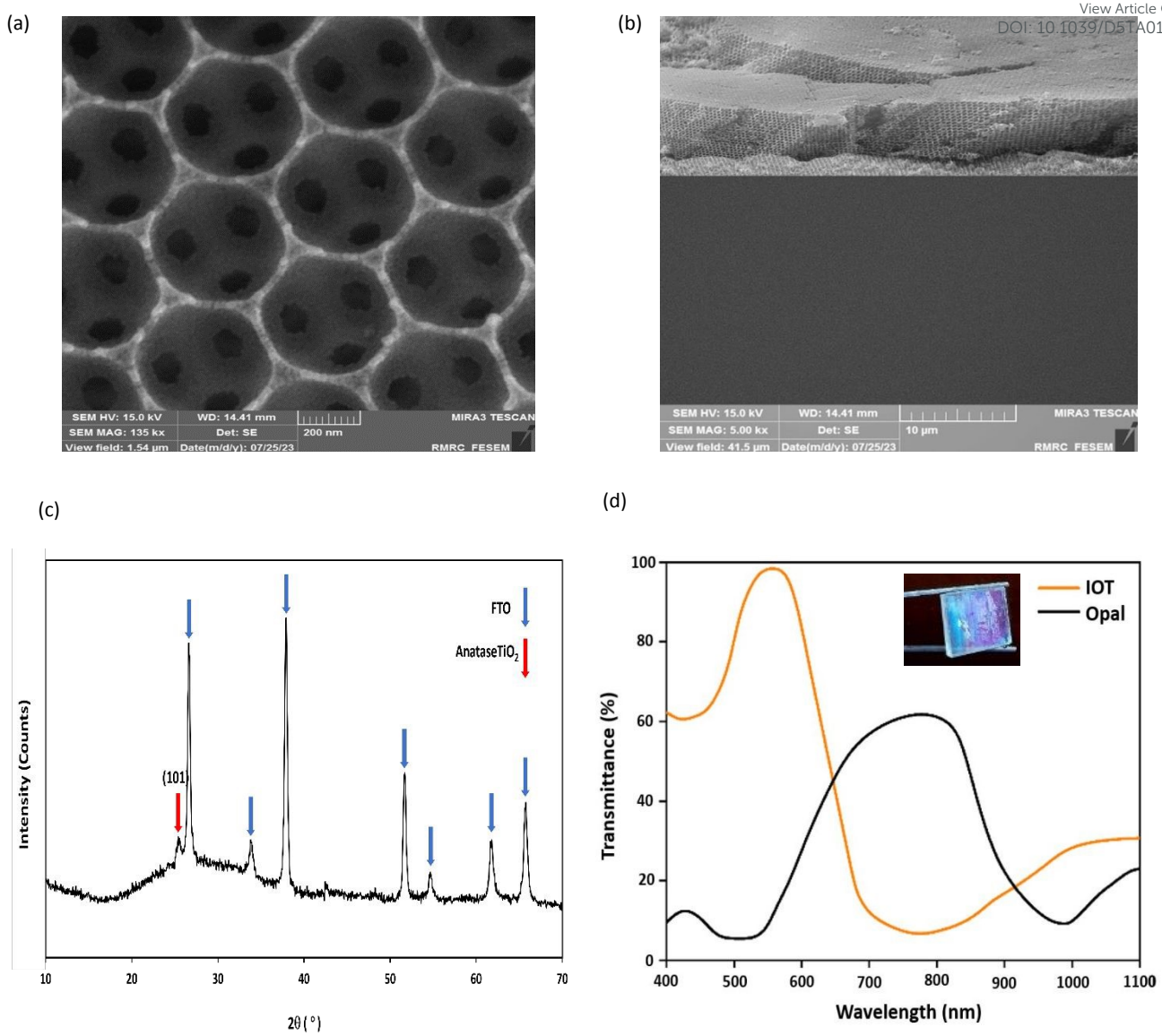

Fig. 2 (a) FE-SEM top-view image and (b) cross-section view of IOT fabricated from 400 nm PS spheres. (c) XRD pattern of IOT deposited on FTO coated glass and (d) Transmittance spectra measured for initial opals PS spheres and IOT. The inset of the Fig. 2d is the camera photograph of the prepared IOT.

Characterization of TiO_2 Inverse Opals (IOT)

TiO_2 inverse opals (IOTs) layers made by liquid-phase deposition (LPD) approach are shown in Fig. 2a and 2b. The empty spaces between polystyrene spheres were filled with TiO_2 solution materials, which, after undergoing a calcination process and removing polystyrene templates, resulted in the formation of voids with an average diameter of around 340 nm. We also analyzed two points of two dissimilar titania inverse opal samples with different resolutions FE-SEM (Fig. S2). The FE-SEM images of inverse opals show a continuous and well-connected TiO_2 network that forms around where the polystyrene spheres used to be. This observation confirms that the titania solution is infiltrated inside the empty spaces.

The contraction occurs because the PS template ruptures and is removed during the calcination process, resulting in a smaller size for IOT relative to the parent colloid crystal template. The XRD pattern of the deposited TiO_2 inverse opal layer on FTO is depicted in Fig. 2c. A peak at 2Θ = 25.3º, attributed to the (101) crystal plane of the anatase phase, can be seen in the structure of IOT. The anatase phase is highly preferred in comparison to other polymorphs for applications in photovoltaics and photoelectrochemistry due to its ability to minimize the recombination rate of electrons and holes [38, 39]. The weak anatase peak is due to the thin, porous, and nanocrystalline structure of the IOT, which reduces crystalline volume and peak intensity [28, 40, 41]. This nanocrystallinity does not compromise the IOT's photonic bandgap, which enhances light confinement and

View Article Online
DOI: 10.1039/D5TA01376C

photon absorption by $CsPbBr_3$ for photoelectrochemical water splitting. The anatase phase ensures efficient charge transport with low electron-hole recombination [39] ".

The formation of opal structure is verified using transmittance spectra measurements. PS opal structures are a well-studied class of photonic bandgap materials and the position of photonic bandgaps can be calculated using modified Bragg equation[42].

$$\lambda = 2d_{111}[n_s^2 f + n_v^2(1-f)]^{1/2} \quad (3)$$

Where

$\lambda = 2\times0.816\times D\times(n_{eff}^2 - Sin^2\vartheta)^{1/2}$

$n_{eff}^2 = (1-f)\times n_{air}^2 + f\times n_{medium}^2$

The bandgap manifest itself in the transmittance spectra as strong reductions in the transmittance. The transmittance measurements of the opal and inverse opal TiO_2 samples are shown in Fig. (d) The spectrum of PS opal sample shows a strong reduction in the 600-900 nm wavelength range. The formula gives 814 nm for the photonic bandgap. However, the broad linewidth of the bandgap can be associated with the i) light interference within the FTO-glass substrate and ii) defects within the photonic crystal. In general, the shape of the transmittance spectra matches well with reported ones in the Literature. Golabi et al. hence confirming formation of PS opal[28]. Moreover, the rainbow colour of the sample is a visual confirmation for formation of a photonic crystal.

The transmittance spectrum of IOT sample shows a strong reduction near 560 nm wavelength. This value again matched the calculated value using formula (3) and is similar to transmittance values reported for inverse opal structures in the Literature[28]. The accuracy of the obtained results was further validated by employing the Bragg equation (Eq. (3)).

Where n_s and n_v are the refractive indexes of the spheres and their surrounding medium, respectively. The refractive indexes for polystyrene (n_{PS}) and air (n_{air}) are 1.6 and1, respectively.

The refractive index range for titanium dioxide ($nTiO_2$) is between 2.2 and 2.6.

Additionally, the filling fraction of the spheres (f) is 0.74 in a closed-packed structure. The equation 4 determines the interplanar spacing d_{111}.

$$d_{111} = \left(\frac{2}{3}\right)^{1/2} D \quad (4)$$

Where *D* is the diameter of the inverse opal or opal spheres [43]. The calculated d_{111} values were 326 and 277 for opal with a diameter of 400 nm and inverse opal with a diameter of 340 nm, respectively. In Fig. 2d, the transmission spectra are displayed for both initial opals and inverse opals. In both cases, there are noticeable dips in transmission, occurring at 967 nm for opal and 790 nm for 3D inverse opal. Remarkably, these values align perfectly with the stop band maximum determined using the Bragg equation (Eq. (3)). However, Fig. 2d provides evidence exhibit a sharp reflectance at the stop band [28, 42]. In addition, as shown in the inset of the Fig. 2d, the synthesized IOT film has a colourful look, attesting to its superior optical quality.

Photoelectrochemical performance of PSC photoanodes based on 3D IOT

The structures of PSC-based photoanodes containing IOT layer used in this study are schematically shown in Fig. 3a and 3b. The FE-SEM image of PSC photoanode in the configurations of Glass/FTO/c-TiO_2/m-TiO_2/IOT/$CsPbBr_3$/Carbon presented in Fig. 3c show the presence of perovskite crystal materials within the IOT macroporous scaffolds (see also individual elemental maps in Fig. S3). From the cross-sectional FE-SEM images, it becomes evident that the LPD infiltration protocol effectively ensures that the perovskite material is uniformly distributed and completely fills the entire porous scaffold made of IOT. The grey circles inside the white perovskite layer confirm the existence of the IOT structure. To quantify the atomic ratios of Cs:Pb:Br in the layer and evaluate whether the infiltration process achieves uniform pore filling or exhibits localized agglomeration/voids, EDS analysis were conducted at three different regions of the cross sectional IOT-$CSPbBr_3$ layer in m-TiO_2/IOT/PVSK sample (Fig. S4, Table S1 and Table S2). As can be seen, the results are very close to the ideal perovskite stoichiometry (1:1:3) and show low standard deviations, indicating a homogeneous distribution of $CsPbBr_3$ within the IOT framework and confirming that our infiltration process yields a uniform and ideal perovskite composition. Notably, the perovskite crystals have grown inside the voids of the IOT scaffold and this can lead to the goal that when light hits the perovskite, it is trapped inside the lattice of the IOT structures and increases light absorption.

To prove the impact of TiO_2 inverse opals on optical properties of $CsPbBr_3$ perovskite materials, UV-vis absorption spectra were measured as illustrated on Fig. 3d. As observed, the optical absorption spectra of the $CsPbBr_3$ films without inverse opal layer exhibit a distinct absorption peak at 515 nm. The absorbance of IOT/PVSK decreases sharply from 515 to 800 nm, consistent with previous reports' results [44]. The influence of inverse opal can best be described by the range of wavelengths between 500 and 1000 nm. Absorption over 1000 nm is parasitic, while below 500 nm the penetration depth is small enough to absorb most of the light within a couple of nanometers without needing any light trapping mechanism [45]. As can be seen, $CsPbBr_3$ perovskite material in the presence of IOT films demonstrate obviously higher absorption than the samples without IOT scaffolds, indicating the IOT structure has a unique impact on the optical properties of the perovskite material. To determine whether loading more $CsPbBr_3$ leads to increased performance or the light scattering by the inverse opal structure, we carried out colorimetry analyses after dissolving loaded $CsPbBr_3$ perovskite in 6M HCl. We estimate the amount of CsPbBr3 loading by measuring the optical absorption of the Pb chloro complex in the solution, which has a strong UV absorbance. In this regard, the m-TiO_2/PVSK and m-TiO_2/IOT/PVSK samples were analyzed and the results are shown in Fig. S5. We can see that, the sample with inverse opal

View Article Online
DOI: 10.1039/D5TA01376C

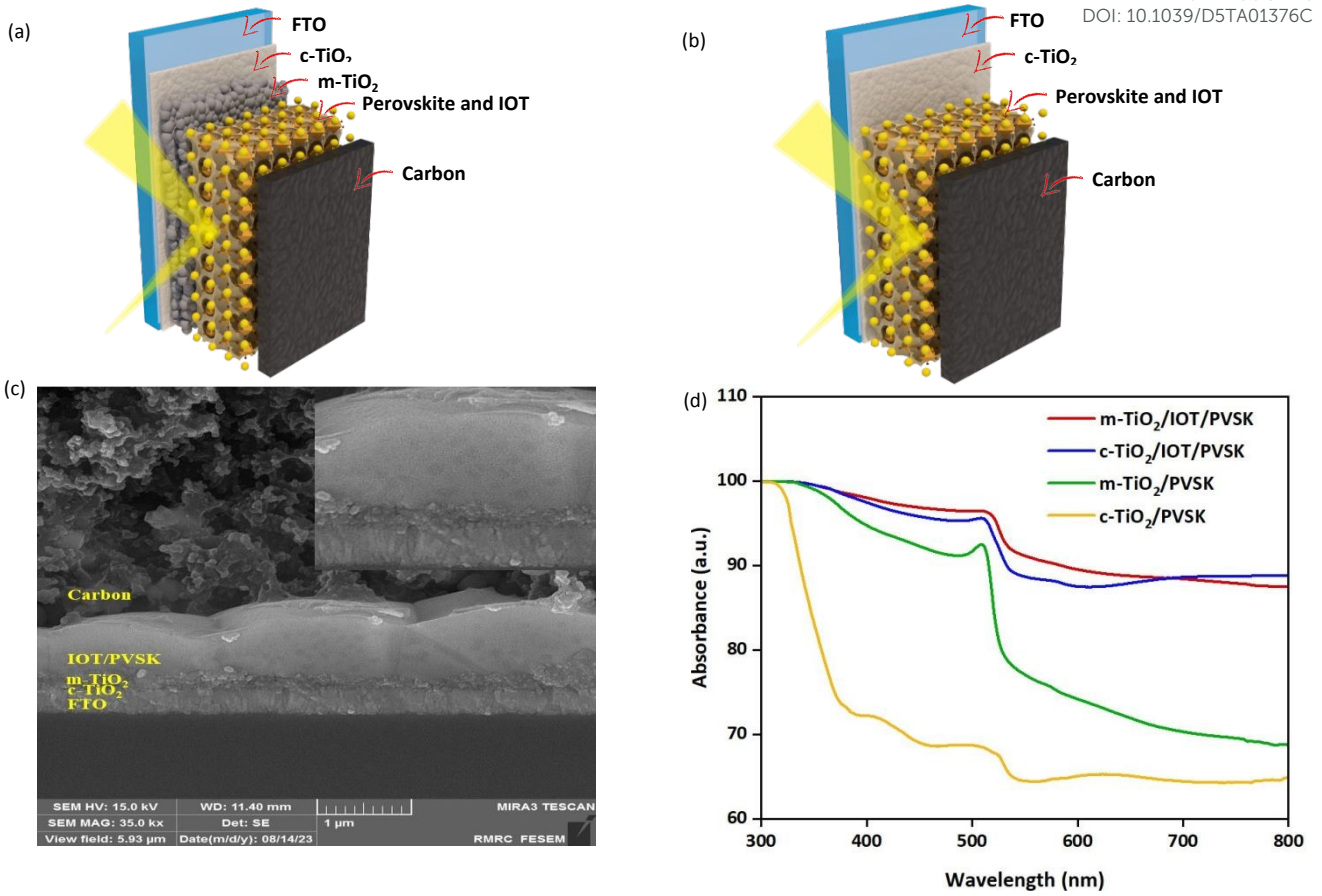

Fig. 3 Schematic of the C-PSC photoanodes containing IOT layer with the configurations of (a) Glass/FTO/c-TiO_2/m-TiO_2/IOT/$CsPbBr_3$/Carbon, (b) Glass/FTO/c-TiO_2/IOT/$CsPbBr_3$/Carbon. (c) A cross-sectional FE-SEM image of the photoelectrode with the configuration of Glass/FTO/c-TiO_2/m-TiO_2/IOT/$CsPbBr_3$/Carbon. Inset shows a zoom view of the photoelectrode. (d) UV-Vis spectra of the $CsPbBr_3$ perovskite materials with and without IOT layers.

has a slightly higher absorbance than the sample without inverse opal after dissolving in 6M HCl. However, the absorption spectra of Fig. 3d show significant differences in optical absorption of the samples with and without IOT, therefore scattering is expected to be dominant effect in the sample with inverse opal. Furthermore, the sub-bandgap optical absorption (not corrected for reflectance) of Fig. 3d is another proof of higher optical scattering in samples with IOT.

Photoelectrochemical measurements to investigate the performance of $CsPbBr_3$ perovskite photoanodes with and without IOT structure in water oxidation are presented in Fig. 4. In this regard, four structures of Glass/FTO/c-TiO_2/m-TiO_2/IOT/$CsPbBr_3$/C, Glass/FTO/c-TiO_2/IOT/$CsPbBr_3$/C, Glass/FTO/c-TiO_2/m-TiO_2/$CsPbBr_3$/C, Glass/FTO/c-TiO_2/$CsPbBr_3$/C were considered as photoanode in water splitting. We named these configurations m-TiO_2/IOT/PVSK, c-TiO_2/IOT/PVSK, m-TiO_2/PVSK and c-TiO_2/PVSK, respectively. None of the four-electrode measured by linear sweep photovoltammetry (LSV) showed any detectable dark current density at current onsets below 1.4 V (vs reversible hydrogen electrode, RHE; Fig. 4a). Visible light illumination condition resulted in the current densities of 1.63, 3.51, 5.19, and 7.28 mA.cm^{-2} at 1.23 V_{RHE} for c-TiO_2/PVSK, m-TiO_2/PVSK c-TiO_2/IOT/PVSK and m-TiO_2/IOT/PVSK samples, respectively. It is worth mentioning that the photocurrent density-voltage (*j-V*) curves of the electrodes containing IOT improved significantly so that m-TiO_2/IOT/PVSK electrode exhibits the highest value. Indeed, in the presence of light, from an onset of about 0.12 V_{RHE}, the photoelectrode consisting of Glass/FTO/c-TiO_2/m-TiO_2/IOT/$CspbBr_3$/Carbon reached 7.28 mA.cm^{-2} at 1.23 V_{RHE}. Such remarkable progress in photocurrent density can be due to the synergetic effect of two factors. Firstly, light scattering, increased light absorption by perovskite materials and consequently increased light harvesting in the presence of the TiO_2 inverse opal structure have increased the performance of this structure. Secondly, in the uniquely designed configuration, both the mesoporous and macroporous (inverse opal) structures of TiO_2 increase the charge separation efficiency due to the enhancement in specific surface areas and thus improve the photocurrent density. These reasons are strengthened by comparing the performance of the four kinds of electrodes. The m-TiO_2/PVSK sample with mesoporous ETL has the higher photocurrent density at 1.23 V_{RHE} compared to the c-TiO_2/PVSK sample without mesoporous ETL. Higher photocurrent density is a result of increased surface area and enhanced charge separations and transport through electron injection into

View Article Online
DOI: 10.1039/D5TA03766

mesoporous TiO_2 [46]. Notably, the c-TiO_2/IOT/PVSK possesses a better performance in comparison to the m-TiO_2/PVSK. This demonstrated that the IOT macroporous structure has a more effective role in increasing the performance of these sample due to increased light scattering compared to the mesoporous titania structure. Moreover, the IOT's 3D porous structure functioning at the electron transport layer, enhances charge separation by integrating $CsPbBr_3$ within an ordered porous network, which significantly shortens the electron transport path from the photoactive $CsPbBr_3$ layer to the TiO_2 scaffold. In fact, the pores inside the IOT, which has been filled by the $CsPbBr_3$, allow the electrons to move much shorter distances to meet the TiO_2 (ETL) and most of the excitons generated at the vicinity of the $CsPbBr_3$/IOT interface experience a charge separation process (Fig. S6). This reduced path length decreases the charge separation distance, minimizing charge recombination and improving carrier collection efficiency [47, 48]. Furthermore, the onset potentials under light were determined to be 0.31 V_{RHE} for c-TiO_2/PVSK and 0.25 V_{RHE} for m-TiO_2/PVSK samples without IOT, and 0.17 V_{RHE} and 0.12 V_{RHE} for c-TiO_2/IOT/PVSK and m-TiO_2/IOT/PVSK, respectively.

Transient photocurrent responses of the samples were acquired by multiple irradiations on-off cycles for further investigation of the PEC-WS performance (fig. 4b). The photocurrent profile shows an initial overshoot that is later relaxes to smaller photocurrents. This behaviour indicates that charges accumulate at the semiconductor electrolyte interface and therefore application of suitable electrocatalysts that facilitate charge injection into the electrolyte may further improve the photocurrent. The photocurrent instantly fell to zero as soon as the light was switched off. The spikes observed in the transient photocurrent responses (Fig. 4b) results from the rapid generation and separation of electron-hole pairs upon illumination, facilitated by the IOT's photonic bandgap, which enhances light absorption by $CsPbBr_3$. Holes migrate to the carbon surface, while electrons are transferred to the conduction band (CB) of TiO_2, leading to a sharp increase in photocurrent [49-52]. The subsequent relaxation to a lower, steady-state photocurrent is due to charge accumulation at the semiconductor-electrolyte interface and partial recombination of holes with electrons from the perovskite's CB or reduced species in the electrolyte. The 3D IOT layer and the anatase TiO_2 phase minimize recombination, improving charge extraction and contributing to the higher anodic photocurrent observed in the m-TiO_2/IOT/PVSK configuration compared to other samples. In fact, a steady current exists when the processes of electron-hole (e/h) separation and recombination are balanced. The photocurrent rapidly drops to zero when the light is switched off because the holes accumulated at the carbon surface and the electrons in the CB of perovskite are recombined at the same time. Fig. 4b illustrates that the photocurrent generation for all samples is quick and reproducible. The synergistic effect responsible for the high photoelectrochemical performance can be traced back to the significantly greater anodic photocurrent of the m-TiO_2/IOT/PVSK compared to other samples. Furthermore, due to the existence of a conductive carbon protective layer, all four types of samples exhibit remarkable stability in the chronoamperometric measurement performed for 10000 s at 1.23 V_{RHE} under continuous illumination, as shown in Fig. 4c. To confirm the structural and chemical stability of $CsPbBr_3$ after operation, X-ray diffraction (XRD) analysis was conducted to ensure that no $PbBr_2$, CsBr, or other decomposition products were present (Fig. S7). XRD characterization was performed on pristine $CsPbBr_3$ without carbon protection before any water exposure, establishing the initial $CsPbBr_3$ crystalline phase. After deposition of the carbon protective layer, the sample underwent chronoamperometric PEC testing for 10,000 s under illumination. Following PEC operation, the carbon layer was removed by washing with ethyl methyl ketone that is the carbon layer solvent, and XRD was conducted again on the exposed perovskite. The post-PEC XRD shows no evidence of $PbBr_2$ or CsBr formation, confirming the absence of bulk degradation.

To reveal the importance of the IOT top layer for light harvesting, the incident photon-to-current conversion efficiency (IPCE) of perovskite-based photoanodes with IOT was compared to those without IOT in a solution of 0.1 M Na_2SO_4 (pH 7) by the use of a bias of 1.23 V_{RHE} (Fig. 4d). All samples exhibit an IPCE dropping to zero near ~575 nm, in good agreement with the respective UV-Vis absorbance spectra (Fig. 3d). The peak wavelengths of the c-TiO_2/PVSK and m-TiO_2/PVSK photoanodes are around 515 nm. When compared to c-TiO_2/PVSK, which displays an IPCE of 14.9% at 515 nm, the m-TiO_2/PVSK photoanode displays considerably higher IPCE of 35.09% at 515 nm, indicating improved charge separation efficiency in the presence of the m-TiO_2 layer. At 415–550 nm, the gain was 2.3-fold as great, confirming that mesoporous TiO_2 is the cause of the enhanced charge separation efficiency. In terms of the increase in IPCE, the m-TiO_2/IOT/PVSK sample exhibited a 2.1-fold higher gain compared to the m-TiO_2/PVSK electrode. Similarly, the c-TiO_2/IOT/PVSK sample showed a 3.5-fold higher gain in IPCE compared to the c-TiO_2/PVSK sample. This significant improvement can be attributed to the presence of IOT, which creates a periodic structure that enables effective light trapping. It is worth noting that this enhancement was not observed in the photoanodes lacking IOT. However, the m-TiO_2/IOT/PVSK photoelectrode has the highest IPCE.

View Article Online
DOI: 10.1039/D5TA01376C

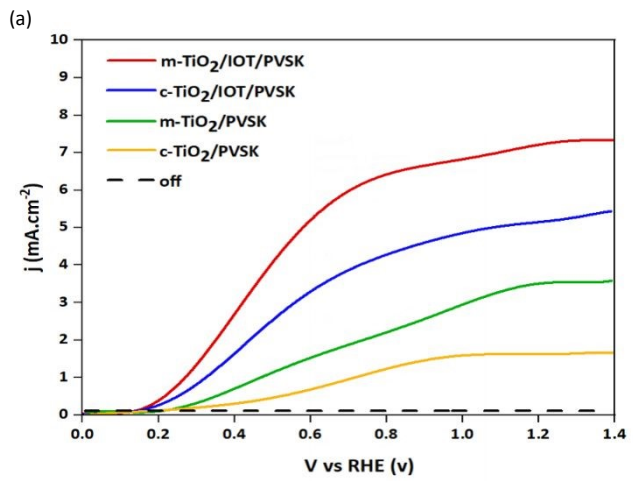

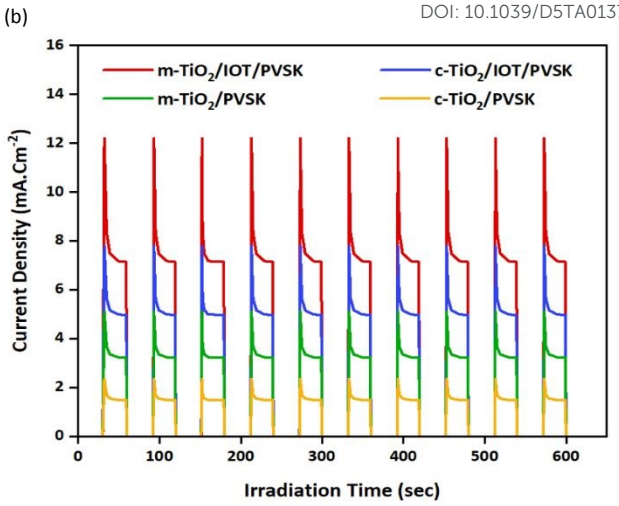

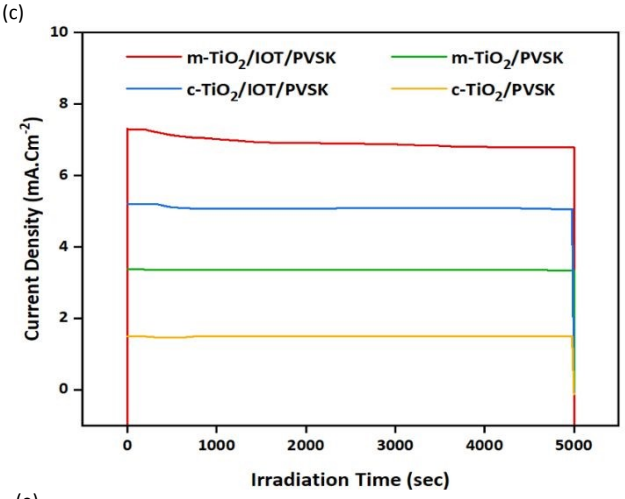

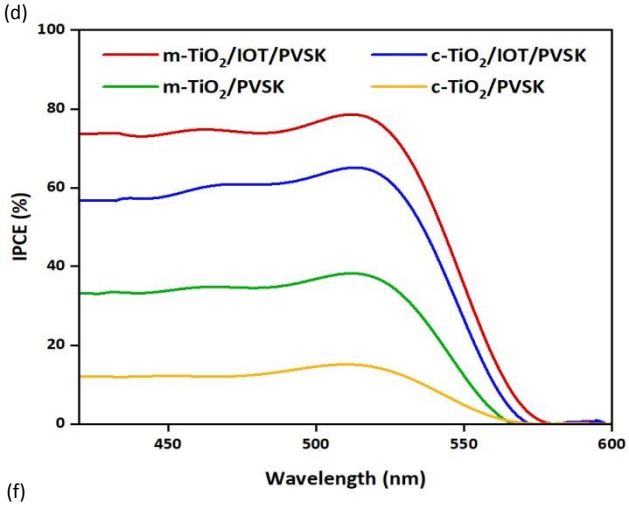

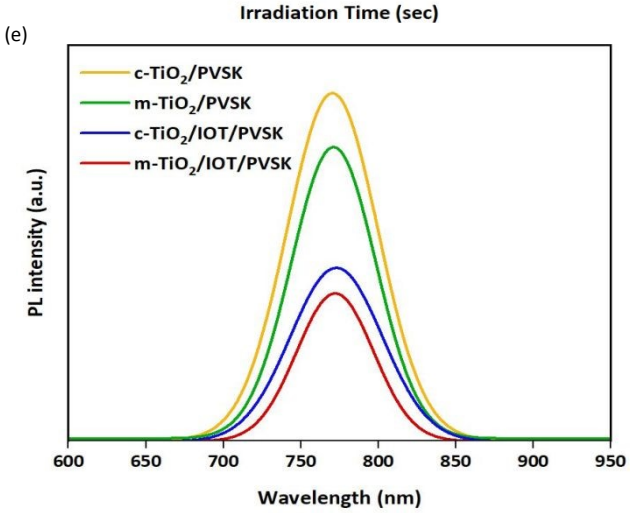

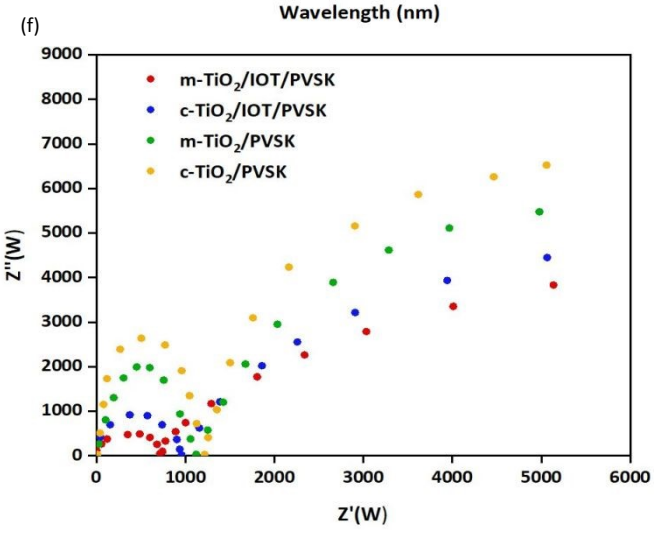

View Article Online
DOI: 10.1039/D5TA01376C

ARTICLE

Fig. 4 (a) LSV measurements of the $CsPbBr_3$ based photoanodes with and without IOT under dark and light conditions in 0.1 M Na_2SO_4 electrolyte at pH 7. (b) Transient PEC measurements of the samples at 1.23 V_{RHE}. (c) Chronoamperometric measurement of photoanodes at 1.23 V_{RHE} under constant illumination (100 mW cm^{-2}) in 0.1 M Na_2SO_4 electrolyte. (d) Wavelength-dependent IPCE spectra at 1.23 V_{RHE}. (e) Photoluminescence spectroscopy of the perovskite based photoanodes with and without IOT, and (f) Impedance analyses (Nyquist plots) of the photoanodes obtained at 1.23 V_{RHE} in 0.1 M Na_2SO_4 electrolyte.

The greater light absorption and charge separation efficiency in this specific sample may be the cause of the better performance. Significantly, the scattering has a major impact on the amplification of the related IPCE activities, which leads to integrated photocurrents from IPCE spectra were determined, and the results showed a good match with the photocurrent density values provided in Fig. 4a. The c-TiO_2/PVSK, m-TiO_2/PVSK, c-TiO_2/IOT/PVSK, and m-TiO_2/IOT/PVSK photoelectrodes displayed integrated photocurrents of 1.54, 3.39, 4.98, and 7.17 mA.cm^{-2} at 1.23 V_{RHE}, respectively.

Photoluminescence (PL) spectroscopy provides information about the band-to-band transition in semiconductors because PL arises from the recombination of these charge carriers. The intensity of PL is directly influenced by the recombination process of these excited electrons and holes. If the PL emission intensity is low, it indicates that the sample has a decreased ability to efficiently recombine these carriers and increased capability of charge separation. As can be seen from the Fig. 4e, the m-TiO_2/PVSK presents a weaker PL intensity in comparison to the c-TiO_2/PVSK probably due to the higher surface area of mesoporous structure and increasing charge separation efficiency. On the other hand, the characteristic emission of photoelectrodes is significantly influenced after the introduction of the IOT layer. This behavior indicates that efficient charge transfer takes place at the interface of the $CsPbBr_3$/IOT heterojunction. Therefore, the IOT layer increases the charge separation efficiency in addition to growing the light-harvesting efficiency.

In order to analyze and compare the migration of charge carriers in c-TiO_2/PVSK, m-TiO_2/PVSK, c-TiO_2/IOT/PVSK, and m-TiO_2/IOT/PVSK photoelectrodes, electrochemical impedance spectroscopy (EIS) was used. The Nyquist plots obtained for each sample exhibited two distinct semicircles (Fig. 4f). The semicircles observed in the low-frequency range correspond to the bulk of the semiconductor and represent the migration of electrons towards the back contact. On the other hand, the semicircles observed in the high-frequency range are related to the hole transfer across the photoelectrode/electrolyte interface, which is crucial for the O_2 evolution process[53]. The high-frequency semicircle observed for IOT-based photoanodes is significantly smaller compared to those without IOT. This can be due to the presence of the IOT/$CsPbBr_3$ junction, enhancing the separation of charges due to higher specific surface area of the samples obtained by the inverse opal nanostructure and allows more holes to remain at the carbon/electrolyte interface. Furthermore, IOT/$CsPbBr_3$ has the ability to absorb a greater number of photons, leading to an accumulation of more holes at the carbon/electrolyte interface. The improved charge separation and light absorption result in a significantly smaller high-frequency semicircle in the m-TiO_2/IOT/PVSK photoanode compared to the m-TiO_2/PVSK photoanode. To further elucidate the impact of carbon layer thickness on charge transfer kinetics, additional electrochemical impedance spectroscopy (EIS) measurements were conducted on the m-TiO_2/IOT/PVSK sample under photoelectrochemical (PEC) water splitting conditions. The carbon layer thickness was varied, with one, two, and three layers corresponding to thicknesses of 42 µm, 83 µm, and 124 µm, respectively, as verified by the profilometry method. The Nyquist plots reveal a dominant semicircle in the high frequency range, attributed to the charge transfer resistance (R_ct) at the $CsPbBr_3$/carbon or carbon/electrolyte interface [54, 55] . For a single carbon layer (42 µm), the smallest semicircle indicates efficient charge transfer. However, increasing the carbon thickness to two layers and three layers results in significantly larger semicircles. This substantial increase suggests that thicker carbon layers introduce higher series resistance, hindering charge transfer to the electrolyte and reducing PEC efficiency (see Figure S8). Our deposition technique for Carbon layer does not allows thinner layers, therefore we were not able to study Carbon layers thinner than 42 µm.

J-V measurements of the m-TiO_2/IOT/PVSK and m-TiO_2/PVSK devices with and without IOT measured as a solar cell under 1 sun illumination show that the inverse opal TiO_2 (IOT) layer significantly enhances both the fill factor (FF) and current density compared to samples without IOT (Fig S9 and Table S3) . The IOT's photonic bandgap improves light confinement, increasing photon absorption by $CsPbBr_3$ and therefore current density, while its porous structure facilitates efficient charge extraction and therefore FF [48, 56-58]. These improvements confirm the IOT's role in overcoming optical absorption and charge transfer limitations of $CsPbBr_3$ for photoelectrochemical water splitting.

View Article Online
DOI: 10.1039/D5TA03376C

Finally, a Faradaic efficiency of > 95% was calculated for the oxygen evolution reaction (OER), underscoring the excellent selectivity of these systems for this process (Fig. S10 (b)).

In general, the synthesis of $CsPbBr_3$ perovskite films can be done by various methods, and many researchers have applied these methods to make $CsPbBr_3$ perovskite films and using them in PEC water splitting. The photocurrents in the literature differ from each other because of the different conditions, materials, electrolyte and pH in the PEC-WS assembly. Therefore, it is hard to compare photocurrent as a precise measure. However, we compared our results with some of the most significant studies that have employed $CsPbBr_3$ perovskite films in PEC-WS (Table 1). Yang et al. made Co-doped perovskite $CsPbBr_3$ QDs by hot injection method. The partial substitution of Pb^{2+} sites by Co^{2+} in Co-doped $CsPbBr_3$ QDs with optimal concentrations increased the QD binding energy, lowered carrier transport barriers, enhanced carrier lifetime and separation, and transport speed [59]. Laishram et al. achieved in situ surface passivation and stabilization of $CsPbBr_3$ nanocrystals by using monolayer graphene carbon nitride (CNM). Carbon nitride-coated $CsPbBr_3$ nanocrystals (CNMBr) were able to enable charge separation through permeation/tunnelling of charges on 2D conductive nanoglasses [1]. Poli et al. employed a commercial thermal graphite sheet and a mesoporous carbon scaffold to wrap $CsPbBr_3$. They showed the grafting of an Ir-based water oxidation catalyst (WOC) on the surface of the graphite sheet (GS) electrolyte, which cathodically alters the onset potential of the composite photoanode because of faster charge transfer [24]. Gong et al. produced Ru-$CsPbBr_3$ QDs by hot injection and shielded them using graphite thermal plates as photoanodes. The effective doping of ruthenium with high catalytic activity not only increased the light absorption but also boosted the carrier separation [60]. Also, Gong et al. suggested a simple hot injection method to enhance the photoelectrocatalytic activity of $CsPbBr_3$ QDs with direct Pd doping for photoelectrocatalytic water splitting. The perovskite crystal structure is stabilized by Pd^{2+} cations with small ionic radius as impurity for $CsPbBr_3$ QDs and as a consequence, the hole transfer barrier is lowered, which facilitates the separation and transport of charge carriers [25]. Dabucci et al. achieved a $CsPbBr_3$-based photoanode with a onset potential of +0.4 V_{RHE} and 8 $mA.cm^{-2}$ current density at +1.23 V_{RHE} for water oxidation [61]. The improved performance is due to a NiFeOOH catalyst efficiently supported on a self-adhesive graphite sheet and enhanced charge transport achieved by phase engineering of $CsPbBr_3$. Zhu et al. presented ultra-stable $CsPbBr_3$ perovskite-based photoanodes, which were fabricated with multifunctional glassy carbon and boron-doped diamond sheets coated with Ni and NiFeOOH nanopyramids [27]. These photoanodes achieve water oxidation onset potentials of nearly +0.4 V_{RHE} and photocurrent densities of nearly 8 $mA.cm^{-2}$ at 1.23 V_{RHE}, which is due to the high conductivity of glassy carbon and boron-doped diamond and the catalytic activity of NiFeOOH. They obtained a current density of 5.4 $mA.cm^{-2}$ at pH 9 without using NiFeOOH, less than 7.28 $mA.cm^{-2}$ obtained at pH 7 for this study.

Table 1 shows a comparison of our results with some of the most important studies that used perovskite $CsPbBr_3$ in PEC-WS.

Table 1. Comparison of our results with studies used the CsPbBr3 perovskite layer in Photoelectrochemical water splitting

The configuration of photoanode	*photocurrent density($mA.cm^{-2}$) at 1.23 V_{RHE}*	*pH*	*Electrolyte*	*Stability*	*Co-catalyst*	*ref*
FTO/c-TiO_2/m-TiO_2/Co-$CsPbBr_3$	1.94	12	KOH	5500 s	Co-doped $CsPbBr_3$	30
FTO/ $CsPbBr_3$/CNM	1.55	-	Na_2SO_4	3 months	CNMBr	1
FTO/c-TiO_2/$CsPbBr_3$/GS/WOC	2.5	12.5	KNO_3	30 h	Ir	29
FTO/c-TiO_2/m-TiO_2/Pd-$CsPbBr_3$ QDs/GS	2.07	13	KOH	1200 s	Pd-doped $CsPbBr_3$	50
FTO/SnO2/$CsPbBr_3$/C/Ps/Ni/NiFeOOH	8 5.4	14 9	NaOH	168h	Ni/NiFeOOH	52
FTO/TiO_2/$CsPbBr_3$/C/Graphite/NiFeOOH	8 5.4	14 9	NaOH	100h	NiFeOOH -	51
FTO/ c-TiO_2/IOT/$CsPbBr_3$/C	5.19	7	Na_2SO_4	10000 s	-	This work
FTO/c-TiO_2/m-TiO_2/ IOT/$CsPbBr_3$/C	7.28	7	Na_2SO_4	10000 s	-	This work

Conclusions

$CsPbBr_3$ has excellent material properties for water splitting however in this article we have shown that its optoelectronic properties can be improved using an inverse opal nanostructure of TiO_2 as the electron transport layer. The inverse opal nanostructure improves the optical absorption of $CsPbBr_3$particularly near the bandgap, mainly due to scattering. Furthermore, it functions as a scaffold collecting the electrons from the perovskite, hence improving electron transport in the electrode. The best device prepared using inverse opal

nanostructure displayed photocurrent density of 7.28 mA.cm^{-2} at 1.23 V_{RHE} due to improvement in optical light absorption of $CsPbBr_3$ in the visible region and charge separation efficiency. By comparing the colorimetric analysis results of the $CsPbBr_3$ perovskite dissolved in 6M HCl and the absorption spectra of the solid samples with and without IOT and containing perovskite, it was found that the light scattering by the inverse opal structure plays a role in the increased performance. On the other hand, photoluminescence (PL) spectroscopy and electrochemical impedance spectroscopy (EIS) confirm the increasing charge separation efficiency in the presence of IOT layers. Therefore, the IOT structures raise the charge separation efficiency in addition to growing the light-harvesting efficiency. Additionally, the presence of a conductive carbon protective layer containing carbon waste toner contributes to the remarkable stability observed in all four sample types during the chronoamperometric measurement conducted for 10,000 s at 1.23 V_S under continuous illumination. This research represents an important achievement for inorganic perovskite-based photoanodes with low optical absorption and stability, which will inspire more research and innovation in PEC-WS.

Data availability

The data supporting this article have been included as part of the Supplementary Information.

Conflicts of interest

There are no conflicts to declare.

Acknowledgements

We acknowledge the Iran National Science Foundation (INSF) for the financial support under project No. 4000748 and the University of Isfahan. We also acknowledge Prof. Tom E. Mallouk from the University of Pennsylvania for some scientific guidance.

References

1. D. Laishram, S. Zeng, K. M. Alam, A. P. Kalra, K. Cui, P. Kumar, R. K. Sharma and K. Shankar, *Applied Surface Science*, 2022, **592**, 153276.
2. K. Başaran, B. U. Topçubaşı and T. Davran-Candan, *Journal of CO2 Utilization*, 2021, **47**, 101492.
3. Y. A. Alli, P. O. Oladoye, O. Ejeromedoghene, O. M. Bankole, O. A. Alimi, E. O. Omotola, C. A. Olanrewaju, K. Philippot, A. S. Adeleye and A. S. Ogunlaja, *Science of the Total Environment*, 2023, **868**, 161547.
4. M. G. Lee, J. W. Yang, H. R. Kwon and H. W. Jang, *CrystEngComm*, 2022.
5. A. H. Abdi, *Environmental Science and Pollution Research*, 2023, **30**, 55782-55798.
6. E. Erdoğan, D. Serin Oktay, M. Manga, H. Bal and N. Algan, *Evaluation Review*, 2023, 0193841X231166973.
7. F. Qureshi, M. Yusuf, H. Ibrahim, H. Kamyab, S. Chelliapan, C. Q. Pham and D.-V. N. Vo, *Environmental Research*, 2023, 115963.
8. K. Jastrzębski and P. Kula, *Materials*, 2021, **14**, 2499.
9. A. Davoodabadi, A. Mahmoudi and H. Ghasemi, *Iscience*, 2021, **24**.
10. C. Sanchez, F. J. Espinos, A. Barjola, J. Escorihuela and V. Compañ, *Polymers*, 2022, **14**, 4500.
11. X. Xu, S. Ji, H. Wang, X. Wang, V. Linkov, P. Wang, L. Pan, G. Wang and R. Wang, *Nanoscale*, 2022, **14**, 16490-16501.
12. T. Kahlstorf, J. N. Hausmann, T. Sontheimer and P. W. Menezes, *Global Challenges*, 2023, 2200242.
13. Z. Fan and W. Xiao, *Angewandte Chemie*, 2021, **133**, 7742-7746.
14. A. Rahbari, M. Ramdin, L. J. Van Den Broeke and T. J. Vlugt, *Industrial & engineering chemistry research*, 2018, **57**, 10663-10674.
15. A. Geetha Bhavani, T. Vats and N. Subba Reddy, *Journal of Nanoscience and Nanotechnology*, 2020, **20**, 3943-3950.
16. J. P. Torella, C. J. Gagliardi, J. S. Chen, D. K. Bediako, B. Colón, J. C. Way, P. A. Silver and D. G. Nocera, *Proceedings of the National Academy of Sciences*, 2015, **112**, 2337-2342.
17. K. Zhao, W. Luo, N. Gallandat, J. Zhang and A. Züttel, *Chimia*, 2021, **75**, 156-156.
18. J. Lin, H. Pan, Z. Chen, L. Wang, Y. Li and S. Zhu, *Chemistry–A European Journal*, 2022, **28**, e202200722.
19. Z. Guo and Z. Liu, *Dalton Transactions*, 2021, **50**, 1983-1989.
20. N. Afzali, R. Keshavarzi, S. Tangestaninejad, S. Gimenez, V. Mirkhani, M. Moghadam and I. Mohammadpoor-Baltork, *Applied Materials Today*, 2021, **24**, 101159.
21. N. Afzali, S. Tangestaninejad, R. Keshavarzi, V. Mirkhani, J. Nematollahi, M. Moghadam, I. Mohammadpoor-Baltork, M. Reimer, S. Olthof and A. Klein, *ACS Sustainable Chemistry & Engineering*, 2020, **8**, 18366-18376.
22. F. Hajisharifi, N. Afzali and R. Keshavarzi, in *Photoelectrochemical Engineering for Solar Harvesting*, Elsevier, 2024, pp. 39-65.
23. N. Afzali and R. Keshavarzi, in *Photoelectrochemical Engineering for Solar Harvesting*, Elsevier, 2024, pp. 67-107.
24. I. Poli, U. Hintermair, M. Regue, S. Kumar, E. V. Sackville, J. Baker, T. M. Watson, S. Eslava and P. J. Cameron, *Nature communications*, 2019, **10**, 2097.
25. W. Gong, Y. Li, Y. Yang, H. Guo and X. Niu, *Journal of Materials Chemistry C*, 2023, **11**, 6963-6970.
26. K. Bienkowski, R. Solarska, L. Trinh, J. Widera-Kalinowska, B. Al-Anesi, M. Liu, G. K. Grandhi, P. Vivo, B. Oral and B. Yılmaz, *ACS catalysis*, 2024, **14**, 6603-6622.
27. Z. Zhu, M. Daboczi, M. Chen, Y. Xuan, X. Liu and S. Eslava, *Nature Communications*, 2024, **15**, 2791.
28. P. Golabi, R. Keshavarzi, V. Mirkhani, M. Moghadam, S. Tangestaninejad, I. Mohammadpoor-Baltork and N. M. Abrams, *Journal of power sources*, 2021, **512**, 230488.
29. D. A. Karajz, L. Halápi, T. Stefaniuk, B. Parditka, Z. Erdélyi, K. Hernádi, C. Cserháti and I. M. Szilágyi, *International Journal of Molecular Sciences*, 2024, **25**, 12996.
30. L. Liu, S. K. Karuturi, L. T. Su and A. I. Y. Tok, *Energy & Environmental Science*, 2011, **4**, 209-215.
31. H. Wang, S. K. Gupta, B. Xie and M. Lu, *Frontiers of Optoelectronics*, 2020, **13**, 50-72.
32. K. Hou, W. Ali, J. Lv, J. Guo, L. Shi, B. Han, X. Wang and Z. Tang, *Journal of the American Chemical Society*, 2018, **140**, 16446-16449.

33. L. Zhang, C. Y. Lin, V. K. Valev, E. Reisner, U. Steiner and J. J. Baumberg, *small*, 2014, **10**, 3970-3978.
34. Z. Zhang, X. Yang, M. N. Hedhili, E. Ahmed, L. Shi and P. Wang, *ACS applied materials & interfaces*, 2014, **6**, 691-696.
35. E. Yablonovitch, *Physical review letters*, 1987, **58**, 2059.
36. M. Al Rammal, K. Akkaoui and L. I. Halaoui, *The Journal of Physical Chemistry C*, 2022, **126**, 6960-6972.
37. X. Chai, H. Zhang and C. Cheng, *Semiconductor Science and Technology*, 2017, **32**, 114003.
38. Y. Bai, I. Mora-Sero, F. De Angelis, J. Bisquert and P. Wang, *Chemical reviews*, 2014, **114**, 10095-10130.
39. R. Keshavarzi, M. Mousavian, M. Omrani, V. Mirkhani, N. Afzali, C. A. Mesa, I. Mohammadpoor-Baltork and S. Gimenez, *Surfaces and Interfaces*, 2023, **38**, 102813.
40. M. Ijaz and M. Zafar, *International Journal of Energy Research*, 2021, **45**, 3569-3589.
41. W. Wang, J. Wang, X. Shi, Z. Yu, Z. Song, L. Dong, G. Jiang and S. Han, *BioResources*, 2016, **11**, 3084-3093.
42. S. Guldin, S. Huttner, M. Kolle, M. E. Welland, P. Muller-Buschbaum, R. H. Friend, U. Steiner and N. Tétreault, *Nano letters*, 2010, **10**, 2303-2309.
43. W. L. Vos, R. Sprik, A. van Blaaderen, A. Imhof, A. Lagendijk and G. H. Wegdam, *Physical Review B*, 1996, **53**, 16231.
44. C.-Y. Huang, C.-C. Wu, C.-L. Wu and C.-W. Lin, *ACS omega*, 2019, **4**, 8081-8086.
45. A. Maho, M. Lobet, N. Daem, P. Piron, G. Spronck, J. Loicq, R. Cloots, P. Colson, C. Henrist and J. Dewalque, *ACS Applied Energy Materials*, 2021, **4**, 1108-1119.
46. S.-Y. Lee, P. Serafini, S. Masi, A. s. F. Gualdrón-Reyes, C. A. Mesa, J. Rodríguez-Pereira, S. Giménez, H. J. Lee and I. n. Mora-Seró, *ACS Energy Letters*, 2023, **8**, 4488-4495.
47. T. Leijtens, B. Lauber, G. E. Eperon, S. D. Stranks and H. J. Snaith, *The journal of physical chemistry letters*, 2014, **5**, 1096-1102.
48. M. Vasilopoulou, A. Soultati, P.-P. Filippatos, A. R. bin Mohd Yusoff, M. K. Nazeeruddin and L. C. Palilis, *Journal of Materials Chemistry C*, 2022, **10**, 11063-11104.
49. A. Dabirian and R. Van De Krol, *Chemistry of Materials*, 2015, **27**, 708-715.
50. F. A. Laskowski, J. Qiu, M. R. Nellist, S. Z. Oener, A. M. Gordon and S. W. Boettcher, *Sustainable Energy & Fuels*, 2018, **2**, 1995-2005.
51. P. Ma and D. Wang, in *Nanomaterials for Energy Conversion and Storage*, World Scientific, 2018, pp. 1-61.
52. L. M. Peter, A. B. Walker, T. Bein, A. G. Hufnagel and I. Kondofersky, *Journal of Electroanalytical Chemistry*, 2020, **872**, 114234.
53. B. Zhang, X. Zhang, X. Xiao and Y. Shen, *ACS Applied Materials & Interfaces*, 2016, **8**, 1606-1614.
54. S. M. Abdulrahim, Z. Ahmad, J. Bahadra and N. J. Al-Thani, *Nanomaterials*, 2020, **10**, 1635.
55. C. Raminafshar, D. Raptis, M. R. Mohammadi and P. Lianos, *Micromachines*, 2019, **10**, 266.
56. C. Yuan, Y. Yang, L. Huang and Y. Xiao, *ACS omega*, 2024, **9**, 9720-9727.
57. S. Zhou, R. Tang and L. Yin, *Advanced Materials*, 2017, **29**, 1703682.
58. F. Sadegh, S. Akin, M. Moghadam, R. Keshavarzi, V. Mirkhani, M. A. Ruiz-Preciado, E. Akman, H. Zhang, M. Amini and S. Tangestaninejad, *Advanced Functional Materials*, 2021, **31**, 2102237.
59. Y. Yang, Y. Li, W. Gong, H. Guo and X. Niu, *Colloids and Surfaces A: Physicochemical and Engineering Aspects*, 2023, **663**, 131083.
60. W. Gong, H. Guo and X. Niu, 2022.
61. M. Daboczi, J. Cui, F. Temerov and S. Eslava, *Advanced Materials*, 2023, **35**, 2304350.

View Article Online
DOI: 10.1039/D5TA01376C

View Article Online
DOI: 10.1039/D5TA01376C

The data supporting this article have been included as part of the Supplementary Information.

Contents:

1. Digital camera image of the $CsPbBr_3$-based photoanode (carbon side) (**Fig. S1**).
2. FE-SEM top-view image of two points of two dissimilar titania inverse opal samples with different resolutions (**Fig. S2**).
3. Cross-sectional FE-SEM image and individual elemental maps of Cs, Pb, Br, Ti, O, Sn and Si (**Fig. S3**).
4. Energy-dispersive X-ray spectroscopy (EDS) spectra of measured at three different regions across the IOT-$CSPbBr_3$ layer (**Fig. S4**).
5. Quantitative elemental composition data of $CsPbBr_3$ in m-TiO_2/IOT/PVSK sample extracted from EDS spectra (**Table S1**).
6. Mean ratios, standard deviations, and ideal ratios for elements Cs, Pb, and Br for $CSPbBr_3$ in m-TiO_2/IOT/PVSK sample (**Table S2**).
7. The absorption spectra of $CsPbBr_3$ perovskite loaded materials dissolved in 6M HCl for the m-TiO_2/PVSK and m-TiO_2/IOT/PVSK samples (**Fig. S5**).
8. Schematic diagram of electron and hole movement inside the IOT and perovskite layer (**Fig. S6**).
9. X-ray diffraction (XRD) patterns of pristine m-TiO_2/IOT/$CsPbBr_3$ before any water exposure as well as the XRD patterns of the same sample after carbon coating, chronoamperometric PEC testing (10,000 s illumination) and removing carbon by ethyl methyl ketone solvent (**Fig. S7**).
10. Impedance analyses (Nyquist plots) of the m-TiO_2/IOT/PVSK photoanodes with different carbon layer thicknesses obtained at 1.23 V_{RHE} in 0.1 M Na_2SO_4 electrolyte (**Fig. S8**).
11. Current-voltage scans of the best m-TiO_2/IOT/PVSK and m-TiO_2/PVSK devices with and without IOT measured as a solar cell under 1 sun illumination. Average performance parameters for seven devices are listed in Table S3 (**Fig. S9**).
12. Average performance parameters for seven perovskite solar cells (**Table S3**).
13. a) Chronoamperometric measurement of a m-TiO_2/IOT/PVSK photoelectrode at 1.23 V vs. RHE under constant illumination (100 mW cm^{-2}) and b) Theoretical (green line) and measured (red triangle) O_2 evolution, along with Faradaic efficiency (blue circles) (**Fig. S10**).
14. Average performance parameters for ten photoelectrodes (**Table S4**).
15. Graphical abstract